JACS
JOURNAL OF THE AMERICAN CHEMICAL SOCIETY
pubs.acs.org/JACS
Article

Atomically Resolved Transition Pathways of Iron Redox

Xiaozhi Liu, Yue Pan, Jianxiong Zhao, Yuhan Wang, Mengshu Ge, Lixiang Qian, Liang Zhang, Lin Gu, Dan Zhou,* and Dong Su*

Cite This: https://doi.org/10.1021/jacs.4c05309
Read Online

ABSTRACT: The redox transition between iron and its oxides is of the utmost importance in heterogeneous catalysis, biological metabolism, and geological evolution. The structural characteristics of this reaction may vary based on surrounding environmental conditions, giving rise to diverse physical scenarios. In this study, we explore the atomic-scale transformation of nanosized Fe_3O_4 under ambient-pressure H_2 gas using in-situ environmental transmission electron microscopy. Our results reveal that the internal solid-state reactions dominated by iron diffusion are coupled with the surface reactions involving gaseous O or H species. During reduction, we observe two competitive reduction pathways, namely $Fe_3O_4 \rightarrow FeO \rightarrow Fe$ and $Fe_3O_4 \rightarrow Fe$. An intermediate phase with vacancy ordering is observed during the disproportionation reaction of $Fe^{2+} \rightarrow Fe^0 + Fe^{3+}$, which potentially alleviates stress and facilitates ion migration. As the temperature decreases, an oxidation process occurs in the presence of environmental H_2O and trace amounts of O_2. A direct oxidation of Fe to Fe_3O_4 occurs in the absence of the FeO phase, likely corresponding to a change in the water vapor content in the atmosphere. This work elucidates a full dynamical scenario of iron redox under realistic conditions, which is critical for unraveling the intricate mechanisms governing the solid−solid and solid−gas reactions.

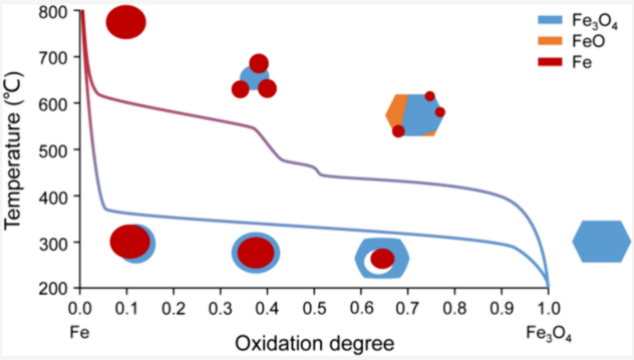

■ INTRODUCTION

The redox reaction of iron is a fundamental process that permeates many aspects of nature. In geology, iron oxides dominate the oxygen exchange interactions with the outgassing volatiles from Earth's interior, leaving a substantial impact on the ancient climate evolution.[1] The historic smelting of metallic iron from ores abundant in iron oxides stands as a cornerstone in the development of human civilization. Today, functionalized iron-based nanoparticles play vital roles in various chemical industries, spanning electrocatalysis, biocatalysis, and thermocatalysis.[2,3] Iron-based catalysts, known for their cost-effectiveness and environmentally benign nature, encounter a challenge with moderate activity, primarily stemming from inherent conflicting factors. For instance, considering the Haber−Bosch process, the synthesis of ammonia inherently favors lower temperatures, which unfortunately leads to oxidative deactivation of the metallic active phase (α-Fe).[4] As a consequence, iron-based catalysts necessitate a prolonged reduction pretreatment to attain the active phase and must operate at elevated temperatures to forestall activity degradation. Certain catalytic challenges stem from the complexities of the phase transitions of catalysts during their operational life span. Therefore, understanding the structural evolution of iron oxides under reducing atmospheres can yield novel perspectives and solutions to address these catalytic hurdles.

It is recently recognized that the metallic catalysts under reaction conditions exhibit nonequilibrium structural variations significantly diverged from their structures at room temperature.[5−7] Significant strides using the in-situ environmental transmission electron microscopy (ETEM) technique have enabled real-time observation of dynamic nonequilibrium structures of catalysts within realistic gas environments at the atomic scale.[8,9] For example, the reduction of Fe_2O_3 or Fe_3O_4 has been previously studied under various environments.[10−14] However, the previous studies focused on redox at high temperatures, where the reaction is kinetically driven and far from practical states. The investigation on the reduction of FeO_x at work conditions is a technically challenging task for ETEM.[15−17] To date, the dynamics of this fundamental reaction remain unclear.

In this work, we investigate the redox transition between iron and its oxides under atmospheric pressure of hydrogen with an optimized gas-cell ETEM technique. As the temperature varies, gas reaction ($H_2 + O_* \rightarrow H_2O_*$) on the surface

Received: April 17, 2024
Revised: June 1, 2024
Accepted: June 3, 2024

ACS Publications

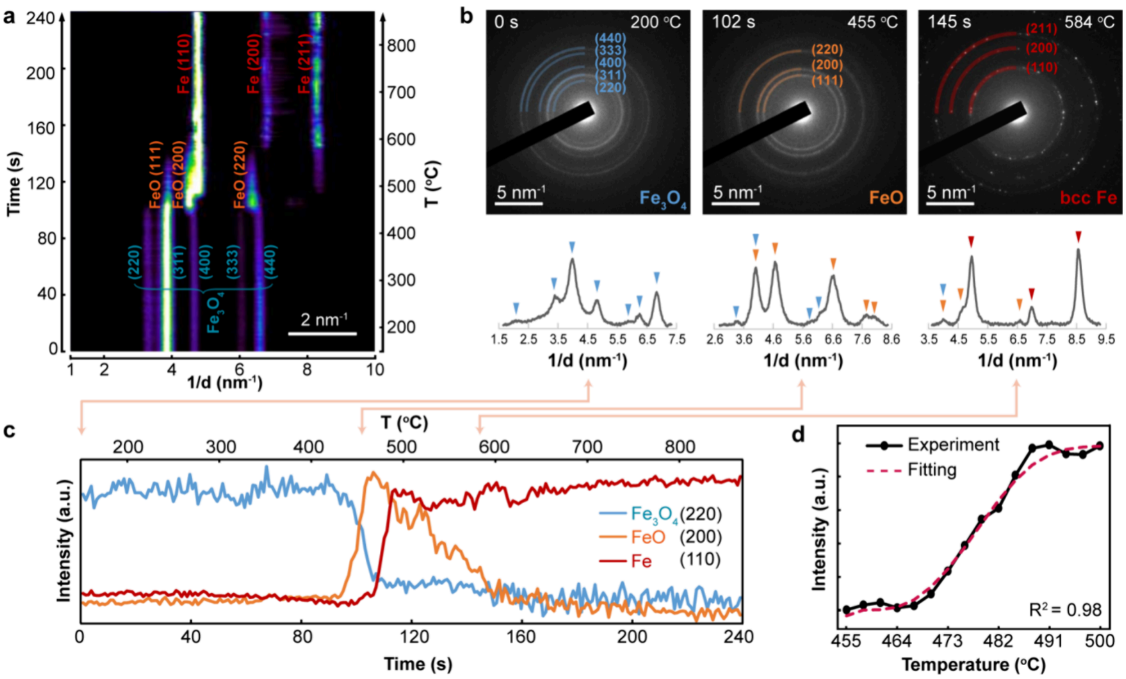

Figure 1. In-situ SAED results during the reduction. (a) Azimuthally integrated SAED intensity map with the distance in the reciprocal space as the *x*-axis, the reaction time as the left *y*-axis, and the temperature as the right *y*-axis. (b) Three typical diffraction patterns at 0 s (200 °C), 102 s (455 °C), and 145 s (584 °C), which can be indexed to Fe_3O_4, a mixture of Fe_3O_4 and FeO, and Fe. (c) Intensity plots of the characteristic peaks from $\{220\}_{Fe_3O_4}$, $\{200\}_{FeO}$, and $\{110\}_{Fe}$, demonstrating their content variations in function of time and temperature. The intensities of the curves have been normalized. (d) Experimental and fitting intensity profile of the $\{110\}_{Fe}$ from 455 to 500 °C.

prompts the iron redox reactions in bulk. Our real-time nanoscale observations show Fe_3O_4 nanoparticles simultaneously undergo different transition pathways as the temperature increases from 347 to 435 °C. The interfacial structures between different phases are systematically characterized. A disproportionation reaction of $Fe^{2+} \rightarrow Fe^0 + Fe^{3+}$ is also found, demonstrating the nonequilibrium nature of the reduction. Surprisingly, while the temperature decreases, iron nanoparticles are directly oxidized to Fe_3O_4 without the presence of FeO. It is suggested that oxidants are the H_2O gas produced from the reduction reaction and trace amounts of the O_2. With the help of density functional theory (DFT) calculations, we find that the redox process of Fe is dominated by the diffusion of iron cations in bulk while the surface reactions with hydrogen simultaneously happen. This work elucidates the kinetic cycles at the atomic scale and deepens our understanding of the mechanisms underpinning the redox reactions of the transition metal oxides.

RESULTS

The dynamic study on the complete reduction of iron oxides has been a long-standing challenge for ETEM techniques due to the requirement of an extremely pure gas environment.[10−17] In principle, even a trace amount of oxidants can impact the equilibrium state of the redox of iron.[18] To optimize the gas environment of the gas cell, we revised the configuration for the entire gas supply system by incorporating leakage-preventing alternatives, such as those constructed from stainless steel or poly(ether−ether−ketone)−silica. Specifically, we meticulously monitor gas leakage using a helium leak detector and reinforce all screws monthly. We always kept the gas supply system in a clean and dry state by flushing and vacuuming the chamber. Our experiments demonstrate that optimizing the gas system can reduce the reduction temperature of Fe_3O_4 by more than 300 °C.

Reduction of the Fe_3O_4 Nanoparticles. We verify with in-situ selected area electron diffraction (SAED) that Fe_3O_4 undergoes a series of phase transitions as the temperature increases from 200 to 800 °C at a rate of 3 °C/s in a hydrogen environment (Figures S1 and S2, Video S1). During this process, three phases sequentially dominate, as indicated in the SAED profile intensity map in Figure 1a. These phases, detailed in Figure 1b, are identified as the magnetite Fe_3O_4 ($Fd\bar{3}m$, JCPDS No. 89-0950, a = 8.40 Å), the wüstite FeO ($Fm\bar{3}m$, JCPDS No. 89-7100, a = 4.31 Å), and the α-Fe ($Im\bar{3}m$, JCPDS No. 89-7194, a = 2.87 Å). The intensities of $\{220\}_{Fe_3O_4}$, $\{200\}_{FeO}$, and $\{110\}_{Fe}$ are plotted in Figure 1c as a function of both time and temperature, offering a qualitative representation of the phase content alterations. The reduction starts at 420 °C as the Fe_3O_4 phase content begins to decrease. From 420 to 470 °C, a decline in the Fe_3O_4 phase is accompanied by the growth of the FeO phase and the Fe phase. Subsequent reduction is supposed to consume the Fe_3O_4 phase rapidly. The Fe phase appears at 450 °C and approaches saturation at ~650 °C. However, a few contents of the Fe_3O_4 phase persist beyond 470 °C and finally diminish at ~630 °C.

Our investigation identifies the presence of the FeO phase within the temperature range of 420−620 °C. According to the Fe−O phase diagram, the appearance of the wüstite phase is expected above 570 °C. However, it is recognized that the gas atmosphere can influence the temperature stability of thermodynamic states, as depicted in the Ellingham diagram (Figure S3).[19,20] Utilizing thermodynamic principles, we scrutinize the impact of residual oxygen and conduct recalculations of the Fe−O phase equilibrium under a

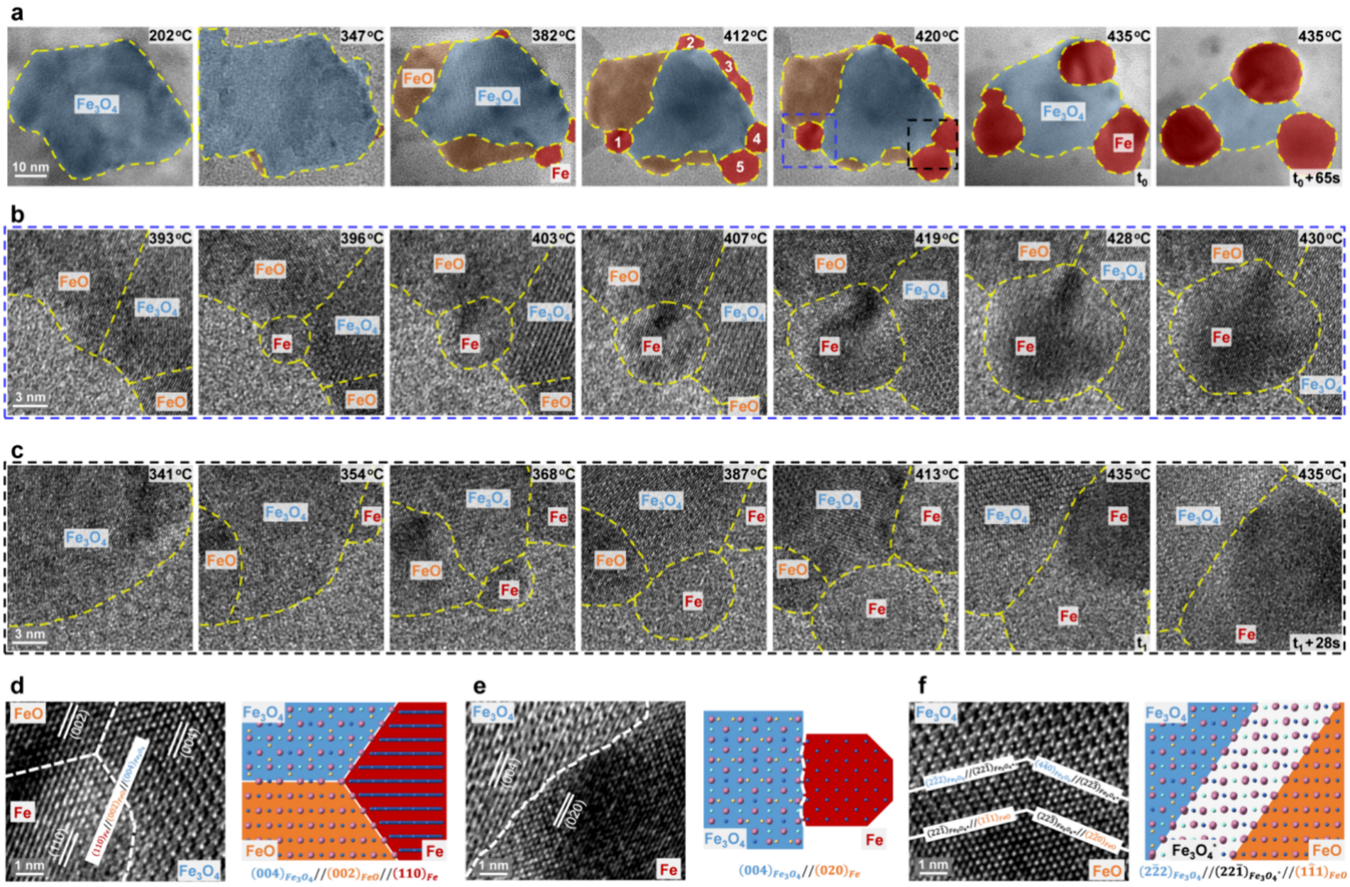

Figure 2. In-situ HRTEM observation during the reduction. (a) Sequential HRTEM images show the reduction behaviors of the Fe_3O_4 nanoparticle as the temperature increases. (b) Enlarged HRTEM images from a selected area (blue dashed box) in (a), showing the nucleation of an iron nanoparticle at the FeO−Fe_3O_4 interface. (C) Enlarged HRTEM images from a selected area (black dashed box) in (a), showing two Fe nanoparticles agglomerated on the surface of the Fe_3O_4 nanoparticle. The phases of Fe_3O_4, FeO, and Fe are indicated by light blue, orange, and dark red, respectively. All of the phase boundaries are indicated by yellow dashed lines. HRTEM images and corresponding atomic models show (d) the three-phase interface among the Fe_3O_4, FeO, and Fe phases, (e) the interface between the Fe_3O_4 and Fe phases, and (f) the intermediate structure between the Fe_3O_4 and FeO phases during the disproportionation reaction. O, light purple. Fe, blue. Half-occupied Fe in the viewing direction, cyan (16d site) or yellow (8a site).

hydrogen atmosphere. Simulation results in Figure S4 substantiate that the presence of hydrogen, water vapor, and residual oxygen can collectively stabilize the FeO phase, enabling its appearance below 570 °C as an intermediate state under specific kinetic conditions, consistent with previous findings.[21−23] This inference is further validated by our in-situ HRTEM results at nonequilibrium conditions. However, the water vapor and oxygen contents are too low to detect by mass spectrometry. Figure 1d shows the intensity curve of the Fe {110} reflections, which aligns well with an Avrami−Erofeyev model. It suggests a mode of nucleation and nuclei growth, where the limiting step is the loss rate of lattice oxygen at the Fe−FeO_x interfaces. At 800 °C, our SAED and EELS results conclusively confirm the complete reduction of Fe_3O_4 to Fe, as depicted in Figures S5 and S6.

In-situ HRTEM results from the same temperature range give further clarification on the phase evolution, as shown in Figure 2a, Figure S7, and Video S2. Fe_3O_4, FeO, and Fe phases can be identified as shown in Figure S8. At lower temperatures, there are some residual ligands on the Fe_3O_4 particles formed from the molecular precursor solution. The ligand−surface interaction may lead to the spreading of Fe_3O_4.[24] As the temperature increases, evaporation of these ligands occurs, leading to the recovery of integrity and crystallinity in the Fe_3O_4 particles. The reduction is initiated at the surface of the Fe_3O_4 particle, fostering independent growth of FeO and Fe nanoparticles (NPs) starting from 347 °C. Between 347 and 357 °C, we observe that the FeO phase grows faster than the Fe phase, consistent with the earlier visibility of diffraction spots of the FeO phase during the in-situ SAED observation. Our observation is different from the commonly believed model where two phases form a shell on the surface of Fe_3O_4.[25] Instead, the FeO phase gradually invades the Fe_3O_4 interior via an interface-migration mode,[26] while the Fe phase grows into larger NPs at the surface of the Fe_3O_4 NP through a classical nucleation-and-growth mode.[27] The FeO phase inherits the morphology of Fe_3O_4 through a topotactic transformation route, which can be attributed to the shared oxygen framework. In contrast, Fe NPs adopt a near-spherical morphology to minimize surface energy. Despite their different nature, two simultaneous transition pathways, Fe_3O_4 → FeO and Fe_3O_4 → Fe, are recognized from the HRTEM imaging. It is interesting that Fe NPs can nucleate not only on the Fe_3O_4 surface but also at the interface between Fe_3O_4 and FeO phases. As shown in Figure 2b and Video S3, with the growth of Fe NPs, both Fe_3O_4 and FeO phases shrink backward, indicating concurrent transitions from the Fe_3O_4 and FeO phases to metallic iron. As enlarged in Figure 2d, a nontrivial

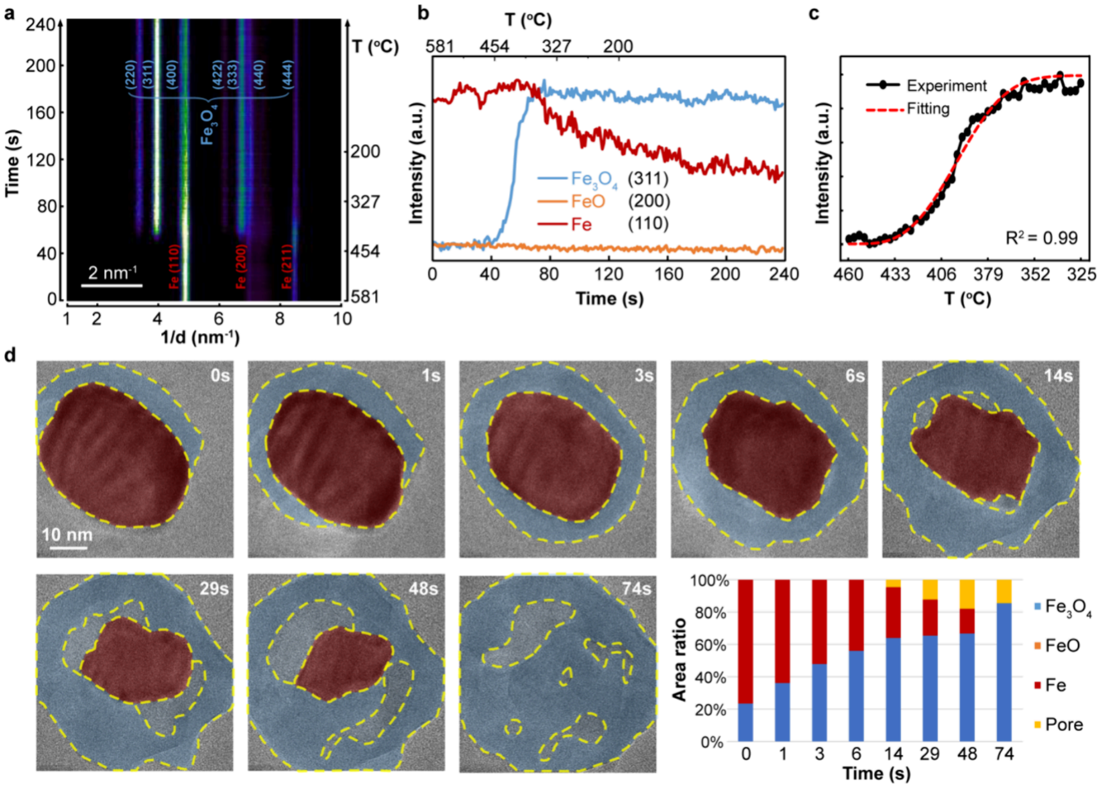

Figure 3. In-situ SAED and HRTEM results during the oxidation. (a) Azimuthally integrated SAED intensity map with the distance in the reciprocal space as the *x*-axis, the reaction time as the left *y*-axis, and the temperature as the right *y*-axis. (b) Intensity plots of the characteristic peaks from $\{311\}_{Fe_3O_4}$, $\{200\}_{FeO}$, and $\{110\}_{Fe}$, demonstrating their content variations with respect to time and temperature. The intensities of the curves have been normalized against the respective phases' maximum values. (c) Experimental and fitting intensity profile of the $\{311\}_{Fe_3O_4}$ from 460 to 325 °C. (d) Sequential HRTEM images show the oxidation behaviors of the Fe nanoparticle as the temperature decreases. The Fe_3O_4 and Fe phases are indicated by light blue and dark red, respectively. All of the interfaces and surfaces are indicated by yellow dashed lines. The projected areas of the phases and pores are presented by percentage stack plots.

three-phase intersection is recognized. The Fe_3O_4 and FeO phases have an orientation relationship of $(2\bar{2}0)_{Fe_3O_4}//(1\bar{1}0)_{FeO}$ and $[110]_{Fe_3O_4}//[110]_{FeO}$. While the Fe particle displays a slight deviation from the zone axis by a few degrees, its $(110)_{Fe}$ crystal planes maintain a parallel alignment with the $(004)_{Fe_3O_4}$ and $(002)_{FeO}$ of the Fe_3O_4 and FeO phases, respectively. Our in-situ results also record the coalescence of Fe NPs on the surface of Fe_3O_4 in Figure 2c and Video S4. During this merging process, the Fe NPs rotate themselves through oriented attachment, similar to the previous observations in liquid cells by in-situ TEM.[28,29] The Fe NP prefers to form on Fe_3O_4 with an orientation relationship, $[110]_{Fe_3O_4}//[100]_{Fe}$ and $(004)_{Fe_3O_4}//(020)_{Fe}$, as shown in Figure 2e.

Disproportionation Reaction of the FeO Phase during the Reduction Process. In addition to the above results, we surprisingly observed a disproportionation reaction from the FeO phase to the Fe and Fe_3O_4 phases (Figure S9). Similar behavior has been reported in the electrochemical reactions of Fe compounds.[30] An intermediate structure intermittently manifests between the FeO and Fe_3O_4 phases, characterized by alternating atomic spacings in adjacent rows, as shown in Figure 2f, Figure S10, and Video S5. This newly formed phase, compared to the FeO phase, exhibits an elevated ordering level of ion arrangement along the $[\bar{1}11]$ direction, resulting in an FFT pattern with a singular pair of ordered diffraction spots (Figure S11). Upon scrutiny within crystallographic databases, we suggest that *Cm* is the most fitting space group for the new phase. Despite its theoretical existence, the Fe_3O_4 (*Cm*) phase has not been experimentally discovered due to its inherently metastable nature.[31] Simulations of the HRTEM images in Figure S12 confirm the structure of this intermediate phase. We speculate that the FeO phase at the FeO−Fe_3O_4 interface maintains the integrity of the oxygen skeleton while releasing one-fourth of the Fe ions, thereby forming this novel Fe_3O_4 (*Cm*) phase (Figure S13). The new phase subsequently transforms to the Fe_3O_4 ($Fd\bar{3}m$) phase in an allotropic way through the redistribution of Fe vacancies. During the disproportionation reaction, these three phases maintain coherent interfaces with an orientation relationship of $(\bar{2}22)_{Fe_3O_4\text{-}Fd\bar{3}m}//(002)_{Fe_3O_4\text{-}Cm}//(\bar{1}11)_{FeO\text{-}Fm\bar{3}m}$. The Fe_3O_4 (*Cm*) as an intermediate phase shows a moderately sized lattice spacing that effectively accommodates the tensile and compressive strains within the Fe_3O_4 ($Fd\bar{3}m$) and FeO ($Fm\bar{3}m$) phases, respectively. Conversely, the latter two phases can serve as stabilizing clamps and facilitate the temporary existence of the Fe_3O_4 (*Cm*) phase, bringing a rare opportunity to experimentally visualize this new phase.

As shown in both in-situ SAED and HRTEM observations, the stability range of the FeO phase is confined within specific temperature bounds. The Fe_3O_4 phase does not entirely transform into the FeO phase during reduction. The complete reduction of the Fe_3O_4 NP to Fe NPs was achieved at 730 °C,

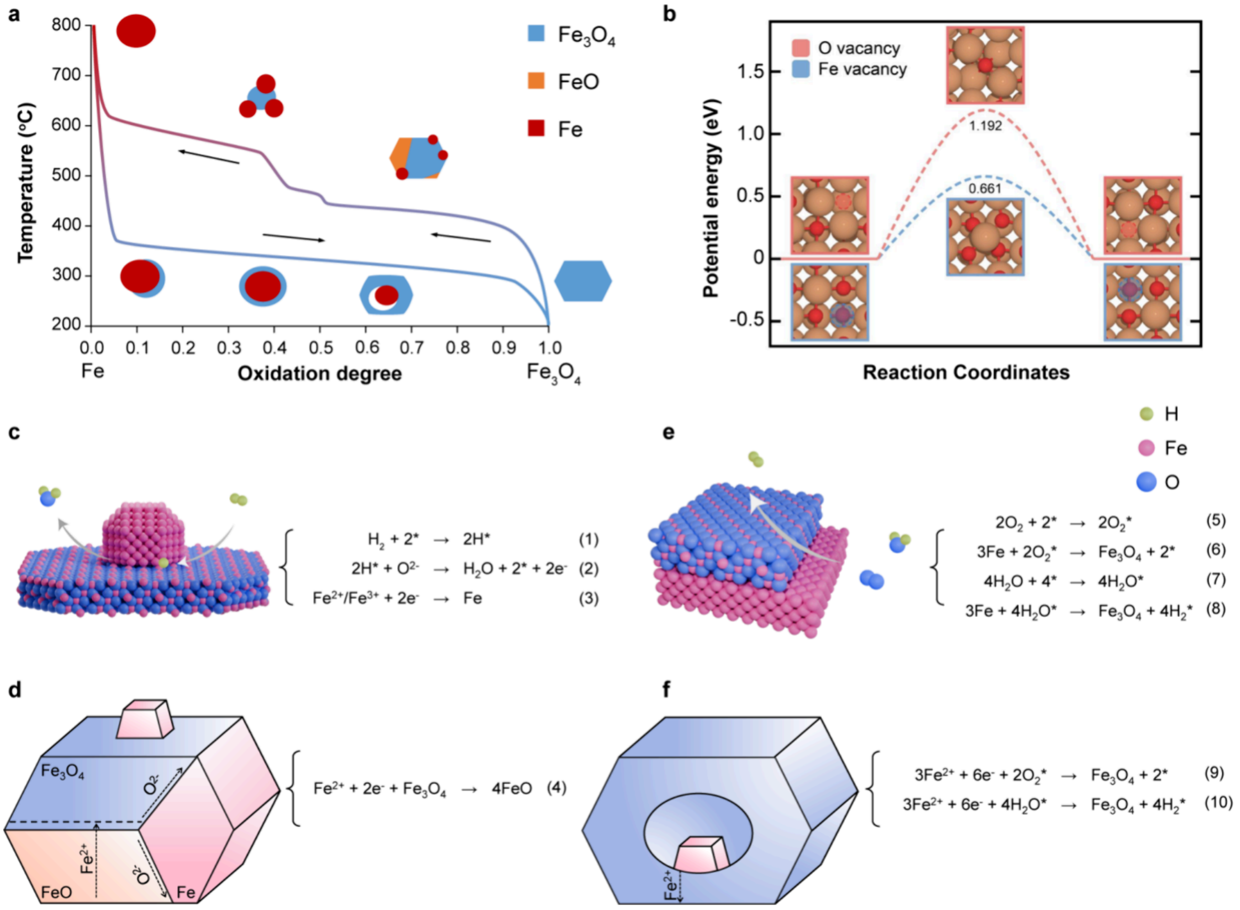

Figure 4. Reaction mechanisms for the redox cycle. (a) Qualitative evolution curve for the oxidation degree of the nanoparticles. Solid arrows indicate the direction of the reactions. (b) DFT calculated energy profile for diffusion of O and Fe vacancies in FeO. Schematic diagrams for the reduction processes (c) at the surface and (d) in the bulk and for the oxidation processes (e) at the surface and (f) in the bulk.

as shown in Figure S8h. Prior studies have highlighted the reduction of Fe_3O_4 follows either a singular one-step pathway (Fe_3O_4−Fe)[32−34] or a consecutive two-step pathway (Fe_3O_4−FeO−Fe).[35−37] Our HRTEM results shed light on this ambiguity by revealing the coexistence of several pathways, which is difficult to find with ensemble-averaging macroscopic methods.[32−37]

Oxidation of the Fe Nanoparticles. We decreased the temperature in the same atmosphere and realized the oxidation transition from metallic α-Fe to Fe_3O_4. The in-situ SAED at the temperature range from 580 to 200 °C with a cooling rate of 3 °C/s is shown in Figure 3a, Figure S14, and Video S6. The oxidation process starts at 460 °C. We deduce that oxygen-containing ingredients, including water vapor generated from the reduction reaction and residual oxygen in the nanoreactor, oxidize Fe to Fe_3O_4. In Figure 3b, the absence of the FeO phase suggests a direct transition pathway from Fe to Fe_3O_4 during the oxidation process. The intensity curve of Fe_3O_4 {311} aligns with an Avrami−Erofeyev model in Figure 3c, suggesting that it adopts a nuclei growth mode similar to that of the Fe phase in Figure 1d. However, the limiting step for oxide growth is the migration of Fe ions across the Fe−Fe_3O_4 interfaces, which is different from the growth of Fe particles.

The oxidation of an isolated Fe NP at 350 °C is shown in the real-space observation of Figure 3d and corresponding Video S7. Fe_3O_4 and Fe phases can be identified as shown in Figure S15. We observe that the Fe_3O_4 phase nucleates on the Fe NP surface, driven by the pronounced affinity of exposed iron for oxidizing gases. The Fe_3O_4 phase progressively expands along the surface of the Fe NP, encapsulating the entire particle within 3 s (stage I) via a classic island growth mode. After an Fe@Fe_3O_4 core−shell structure is formed, the shell layer hinders the direct reaction between the internal iron and gaseous oxidants. At stage II (from 3 to 6 s), the Fe_3O_4 phase grows thicker uniformly. As suggested by the Cabrera−Mott theory,[38] both Fe and O ions permeate the oxide film propelled by the built-in electric field.[39−42] As the oxidation progresses, the outward diffusion of Fe ions will outweigh the inward diffusion of the O ions, resulting in a net outward mass flow. In consequence, voids manifest at the metal−oxide interface, evident at 14 s, attributed to the Kirkendall effect.[43−46] Subsequently, at stage III (from 14 to 74 s), the metallic Fe in the core is oxidized while the Fe@Fe_3O_4 core−shell structure transfers into a porous Fe_3O_4 NP. The statistical result of the projected area of these phases in Figure 3d shows that the content of Fe continuously decreases as the nanoparticle evolves eventually into a porous structure.

■ DISCUSSION

Effect of Water Vapor and Oxygen. In an environment dominated by hydrogen, reduction processes are typically anticipated. However, we observe that the oxidation of iron happens in the same atmosphere as the temperature decreases. It is well-recognized that both water vapor and residual oxygen exist in the H_2-rich atmosphere and serve as oxidizing agents. The oxygen chemical potential in the atmosphere increases as the temperature decreases. Consequently, even in a predominantly H_2 environment, metallic Fe becomes susceptible to oxidation. When the temperature is sustained at 350 °C, the metallic Fe NP can be completely oxidized (Figure 3d). However, as the temperature is rapidly reduced to 200 °C, a portion of the Fe phase is preserved (Figure 3b). This is because the kinetics become markedly sluggish at lower temperatures, failing to surmount the activation barrier for iron oxidation in such a reducing atmosphere. This inspires effective strategies—such as rapid cooling and low-temperature storage—to preserve the metallic state of active materials for further synthetic or catalytic applications.

Asymmetric Redox Cycle. During the entire oxidation process, the FeO phase is absent, which is confirmed in both the in-situ SAED and HRTEM results. There could be two possible reasons: One reason is the change in the gas environment of the system. When the mixture was cooled, some water condenses in the corners of the cold zone of the nanoreactor, reducing the concentration of water vapor around the particles. This is not conducive to the generation of the FeO phase at low temperatures. In the literature, whether the FeO phase exists has been attributed to the content level of water vapor.[21,23,47] The existence of the FeO phase during reduction and the absence of the FeO phase during oxidation reflect different water vapor contents in the nanoreactor. Furthermore, if we consider the interfacial stress between FeO and Fe, it is apparent that the Fe−FeO interface endures a greater strain compared to the Fe−Fe_3O_4 interface. Taken this $(004)_{Fe_3O_4}//(002)_{FeO}//(110)_{Fe}$ orientation relationship as an example, the interfacial lattice mismatch between the Fe and FeO phases (6.2%) is notably larger compared to that between the Fe and Fe_3O_4 phases (3.4%). When subjected to the same energy difference, Fe particles have a tendency to oxidize directly into Fe_3O_4, bypassing the intermediate process of forming the FeO phase. Therefore, the hysteresis observed in the redox behaviors of Fe is primarily kinetic in nature,[48] engendering a pronounced asymmetry between the reduction and oxidation processes within the same gaseous atmosphere. As depicted in Figure 4a, the degree of oxidation of the Fe−O system varies with temperature during the redox cycle. Compared to the reduction process, the spatial distribution of oxides is reversed from inside to outside. This alteration in morphological evolution is intricately related to the ion diffusion dynamics and further influences the redox behaviors of the system.

Mechanisms for the Redox Reactions. Our work indicates that surface reactions affect the structural evolution of iron oxides. The DFT calculation shows the diffusion barrier of Fe vacancy is significantly lower than that of O vacancy in the FeO bulk, suggesting that the dominant factor influencing ionic migrations in the FeO bulk is the mobility of Fe vacancies (Figure 4b). Via ionic diffusion, the surface reaction and phase transition of iron oxides are connected. We present atomic models illustrating the structural evolutions of the entire redox cycle in Figures 4c−f. The reduction initiates at the surface of Fe_3O_4 nanoparticles, where lattice oxygen reacts with hydrogen to generate water vapor (eqs 1 and 2), leaving behind undercoordinated Fe ions. These undercoordinated Fe ions acquire electrons from the reacted oxygen ions (eq 3) and aggregate to form a metallic iron NP at the oxide surface (Figure 4c). Simultaneously, more oxygen ions migrate along the metal−oxide interfaces to react with hydrogen on the surface (eq 2). As the Fe NP grows larger, the spilling of hydrogen atoms over the Fe NP can further accelerate the reduction reaction at the metal−oxide interfaces (eq 1). Additionally, driven by chemical potential, extra coordination-unsaturated Fe ions migrate from the outermost surface to the subsurface and annihilate with Fe vacancies at the 16c Wyckoff sites of the Fe_3O_4 phase. Concomitantly, the Fe ions in the subsurface shift from 8a Wyckoff sites (Fe_3O_4) to 4a Wyckoff sites (FeO), leading to the reduction from the Fe_3O_4 phase to the FeO phase (eq 4). With the increase in the FeO phase, the surface Fe ions need to traverse the as-formed FeO phase to migrate inward and continue to annihilate with the Fe vacancies in the Fe_3O_4 phase, resulting in a forward-advancing FeO−Fe_3O_4 interface (Figure 4d). Therefore, a dynamic coupling is established between the loss of surface oxygen and the decrease in internal Fe vacancies at the FeO−Fe_3O_4 interface. In this scenario, the reduction reaction occurs on the surface, while the structural phase transition occurs inside the particles. As the temperature further increases, the FeO phase starts to decrease due to both thermodynamic and kinetic factors. The FeO phase either transforms to Fe at the surface by losing oxygen or transfers to Fe and Fe_3O_4 phases through a disproportionation reaction. Eventually, the oxide NP loses all of its oxygen and turns into a pure metallic Fe phase. Throughout the reduction process, Fe ions transport and rearrange within the bulk without destroying the oxygen skeleton, adhering to the principle of minimizing the reconstruction of Fe−O bonds. As H_2 reacts with the oxygen from Fe_3O_4 NPs, H_2O is generated and potentially absorbed at the cold surfaces in the nanoreactor, facilitating the oxidation process. When the temperature decreases, the Fe phase oxidizes but does not return along the original pathways, raising a hysteresis between the reduction and the oxidation processes, as shown in Figure 4a. Surface Fe atoms directly react with residual oxygen (eqs 5 and 6) and/or water vapor (eqs 7 and 8), forming an oxide film that encapsulates the Fe particle (Figure 4e). Further oxidation relies on ion transport across the oxide layer. Because of the faster migration of Fe ions compared to O ions, Fe ions gradually diffuse outward under the driving force of the surface oxygen chemical potential and react with the residual oxygen (eq 9) and/or water vapor (eq 10). Consequently, inner voids form as a manifestation of the Kirkendall effect. With the appropriate temperature and sufficient time, the Fe phase is fully converted into the Fe_3O_4 phase (Figure 4f). As a result, a complete reduction−oxidation cycle process of Fe_3O_4 is achieved by heating and cooling in a hydrogen atmosphere.

■ CONCLUSION

In summary, we investigated the atomic-scale redox behaviors of iron oxides by in-situ environmental TEM. We discerned the reduction of Fe_3O_4 to Fe through two concurrent pathways in a H_2 atmosphere at ambient pressure. In the scenario revealed in our work, the reduction reaction occurred on the surface, while the structural phase transition occurred inside the particles. A disproportionation reaction of FeO also participated in the reduction process, leading to the emergence of a novel Fe_3O_4 (*Cm*) phase. As the temperature decreased, oxidation of Fe back to Fe_3O_4 was observed within this H_2-dominant atmosphere because the increased reactivity of water vapor and residual oxygen can serve as oxidants at low temperatures. We found Fe ions can diffuse much faster than O ions within the iron oxides. This disparity in diffusion rates resulted in the predominance of iron diffusion not only in driving the migration of the FeO−Fe_3O_4 interface during the reduction process but also in generating Kirkendall nanopores at the Fe−Fe_3O_4 interface during the oxidation process. The phase transformations observed during these redox processes can be interpreted within the coupling of solid−solid and solid−gas reactions. The complex scenarios and unusual redox hysteresis indicate that the reaction kinetics are influenced by physical factors, including temperature, ion diffusion rate, lattice strain, and the gas atmosphere. This brings out various combinations of coexisting phases and multiple phase interfaces with preferential crystallography orientation relationships. Our results underscore the complexity of iron oxide redox under realistic conditions and illuminate their critical roles in a wide spectrum of reactions, offering profound implications for the fields of catalysis and solid-state chemistry.

■ ASSOCIATED CONTENT

Supporting Information

The Supporting Information is available free of charge at https://pubs.acs.org/doi/10.1021/jacs.4c05309.

Video S1: in-situ SAED video during the reduction process (MP4)

Video S2: in-situ HRTEM video during the reduction process (MP4)

Video S3: enlarged HRTEM video shows an Fe nanoparticle nucleates at the FeO−Fe_3O_4 interface (MP4)

Video S4: enlarged HRTEM video shows two Fe nanoparticles nucleated at different sites grow and agglomerate together (MP4)

Video S5: enlarged HRTEM video shows the evolution of the interfacial structure between the FeO and Fe_3O_4 phases during the disproportionation reaction (MP4)

Video S6: in-situ SAED video during the oxidation process (MP4)

Video S7: in-situ HRTEM video during the oxidation process (MP4)

Figures S1−S15 (PDF)

■ AUTHOR INFORMATION

Corresponding Authors

Dan Zhou − *Beijing National Laboratory for Condensed Matter Physics, Institute of Physics, Chinese Academy of Sciences, Beijing 100190, China; DENSsolutions B.V., Delft 2628 ZD, The Netherlands*; Email: dan.zhou@ikz-berlin.de

Dong Su − *Beijing National Laboratory for Condensed Matter Physics, Institute of Physics, Chinese Academy of Sciences, Beijing 100190, China; University of Chinese Academy of Sciences, Beijing 100049, China*; orcid.org/0000-0002-1921-6683; Email: dongsu@iphy.ac.cn

Authors

Xiaozhi Liu − *Beijing National Laboratory for Condensed Matter Physics, Institute of Physics, Chinese Academy of Sciences, Beijing 100190, China*; orcid.org/0000-0001-8647-8694

Yue Pan − *Beijing National Laboratory for Condensed Matter Physics, Institute of Physics, Chinese Academy of Sciences, Beijing 100190, China; University of Chinese Academy of Sciences, Beijing 100049, China*

Jianxiong Zhao − *Beijing National Laboratory for Condensed Matter Physics, Institute of Physics, Chinese Academy of Sciences, Beijing 100190, China*

Yuhan Wang − *Beijing National Laboratory for Condensed Matter Physics, Institute of Physics, Chinese Academy of Sciences, Beijing 100190, China; University of Chinese Academy of Sciences, Beijing 100049, China*

Mengshu Ge − *Beijing National Laboratory for Condensed Matter Physics, Institute of Physics, Chinese Academy of Sciences, Beijing 100190, China*

Lixiang Qian − *Center for Combustion Energy, School of Vehicle and Mobility, Tsinghua University, Beijing 100084, China*

Liang Zhang − *Center for Combustion Energy, School of Vehicle and Mobility, Tsinghua University, Beijing 100084, China*; orcid.org/0000-0002-9718-0436

Lin Gu − *Beijing National Center for Electron Microscopy and Laboratory of Advanced Materials, School of Materials Science and Engineering, Tsinghua University, Beijing 100084, China*

Complete contact information is available at: https://pubs.acs.org/10.1021/jacs.4c05309

Author Contributions

X.L., Y.P., and J.Z. contributed equally to this work.

Notes

The authors declare no competing financial interest.

■ ACKNOWLEDGMENTS

This work was supported by the National Natural Science Foundation of China (No. U21A20328, 52101277, 22105220, and 22209202), the Strategic Priority Research Program (B) (No. XDB33030200) of Chinese Academy of Sciences, and the Project Funded by China Postdoctoral Science Foundation (No. 2021M703457).

■ REFERENCES

(1) Trail, D.; et al. The oxidation state of Hadean magmas and implications for early Earth's atmosphere. *Nature* **2011**, *480*, 79−82.

(2) Gao, L.; et al. Intrinsic peroxidase-like activity of ferromagnetic nanoparticles. *Nat. Nanotechnol.* **2007**, *2*, 577−583.

(3) Wu, J.; et al. Nanomaterials with enzyme-like characteristics (nanozymes): next-generation artificial enzymes (II). *Chem. Soc. Rev.* **2019**, *48*, 1004−1076.

(4) Kandemir, T.; et al. The Haber-Bosch process revisited: On the real structure and stability of "ammonia iron" under working conditions. *Angew. Chem., Int. Ed.* **2013**, *52*, 12723−12726.

(5) Zhao, Y.; et al. α-Fe_2O_3 as a versatile and efficient oxygen atom transfer catalyst in combination with H_2O as the oxygen source. *Nat. Catal.* **2021**, *4*, 684−691.

(6) Fu, Q.; et al. Interface-confined oxide nanostructures for catalytic oxidation reactions. *Acc. Chem. Res.* **2013**, *46*, 1692−1701.

(7) Zhang, X.; et al. Reversible loss of core-shell structure for Ni-Au bimetallic nanoparticles during CO_2 hydrogenation. *Nat. Catal.* **2020**, *3*, 411−417.

(8) Tang, M.; et al. Recent progresses on structural reconstruction of nanosized metal catalysts via controlled-atmosphere transmission electron microscopy: a review. *Acs. Catal.* **2020**, *10*, 14419−14450.

(9) Zhou, D.; et al. An odyssey to operando environmental transmission electron microscopy: What's next? *Next. Mater.* **2023**, *1*, 100007.

(10) Almeida, T. P.; et al. Insights from in situ and environmental TEM on the oriented attachment of alpha-Fe_2O_3 nanoparticles during alpha-Fe_2O_3 nanorod formation. *CrystEngComm* **2014**, *16*, 1540−1546.

(11) Meng, S.; et al. Irradiation and size effects on redox reaction mechanisms in iron oxides. *Chem. Mater.* **2021**, *33*, 1860−1866.

(12) Zhang, X.; et al. Atomic structure of the Fe_3O_4/Fe_2O_3 interface during phase transition from hematite to magnetite. *Inorg. Chem.* **2023**, *62*, 12111−12118.

(13) Zhu, W. H.; et al. Atomic structural evolution during the reduction of alpha-Fe_2O_3 nanowires. *J. Phys. Chem. C* **2016**, *120*, 14854−14862.

(14) Zhu, W. H.; et al. In situ atomic-scale probing of the reduction dynamics of two-dimensional Fe_2O_3 nanostructures. *ACS Nano* **2017**, *11*, 656−664.

(15) Coombes, M. J.; et al. Iron-silica interaction during reduction of precipitated silica-promoted iron oxides using in situ XRD and TEM. *Appl. Catal. A-Gen.* **2021**, *613*, 118031.

(16) Gai, P. L.; et al. Electron microscopy studies relating to methanol oxidation over ferric molybdate and molybdenum trioxide catalysts. *J. Catal.* **1985**, *94*, 79−96.

(17) Nielsen, M. R.; et al. Reduction and carburization of iron oxides for Fischer−Tropsch synthesis. *J. Energy. Chem.* **2020**, *51*, 48−61.

(18) Goodwin, C. M.; et al. Operando probing of the surface chemistry during the Haber−Bosch process. *Nature* **2024**, *625*, 282−286.

(19) Paul, A. Effect of thermal stabilization on redox equilibria and color of glass. *J. Non-Cryst. Solids* **1985**, *71*, 269−278.

(20) Luo, S.; et al. Chemical looping technology: oxygen carrier characteristics. *Annu. Rev. Chem. Biomol.* **2015**, *6*, 53−75.

(21) Thune, P.; et al. The effect of water on the stability of iron oxide and iron carbide nanoparticles in hydrogen and syngas followed by in situ X-ray Absorption spectroscopy. *J. Phys. Chem. C* **2012**, *116*, 7367−7373.

(22) Pineau, A.; et al. Kinetics of reduction of iron oxides by H_2 - Part I: Low temperature reduction of hematite. *Thermochim. Acta* **2006**, *447*, 89−100.

(23) Zielinski, J.; et al. Reduction of Fe_2O_3 with hydrogen. *Appl. Catal. A-Gen.* **2010**, *381*, 191−196.

(24) Yang, J.; et al. Formation of two-dimensional transition metal oxide nanosheets with nanoparticles as intermediates. *Nat. Mater.* **2019**, *18*, 970−976.

(25) Alalwan, H. A.; et al. α-Fe_2O_3 nanoparticles as oxygen carriers for chemical looping combustion: an integrated materials characterization approach to understanding oxygen carrier performance, reduction mechanism, and particle size effects. *Energy Fuels* **2018**, *32*, 7959−7970.

(26) Fang, H.; et al. A novel 3D mixed-mode multigrain model with efficient implementation of solute drag applied to austenite-ferrite phase transformations in Fe-C-Mn alloys. *Acta Mater.* **2021**, *212*, 116897.

(27) Rogilo, D. I.; et al. Critical terrace width for two-dimensional nucleation during Si growth on Si(111)-(7 × 7) surface. *Phys. Rev. Lett.* **2013**, *111*, No. 036105.

(28) Li, D.; et al. Direction-specific interactions control crystal growth by oriented attachment. *Science* **2012**, *336*, 1014−1018.

(29) Liao, H.-G.; et al. Real-time imaging of Pt_3Fe nanorod growth in solution. *Science* **2012**, *336*, 1011−1014.

(30) He, K.; et al. Sodiation via heterogeneous disproportionation in FeF_2 electrodes for sodium-ion batteries. *ACS Nano* **2014**, *8*, 7251−7259.

(31) Data retrieved from the Materials Project for Fe_3O_4 (mp-612405) from database version v2023.11.1.

(32) Shafiefarhood, A.; et al. Fe_2O_3@$La_xSr_{1-x}FeO_3$ core-shell redox catalyst for methane partial oxidation. *ChemCatChem* **2014**, *6*, 790−799.

(33) Unmuth, E. E.; et al. Iron alloy Fischer−Tropsch catalysts: I. Oxidation-reduction studies of the Fe-Ni system. *J. Catal.* **1980**, *61*, 242−255.

(34) Magnacca, G.; et al. Structural and surface characterization of pure and sulfated iron oxides. *Chem. Mater.* **2003**, *15*, 675−687.

(35) Wagner, D.; et al. A laboratory study of the reduction of iron oxides by hydrogen. *Sohn International Symposium on Advanced Processing of Metals and Materials.* **2006**, 111−120.

(36) Li, K.; et al. Direct conversion of methane to synthesis gas using lattice oxygen of CeO_2-Fe_2O_3 complex oxides. *Chem. Eng. J.* **2010**, *156*, 512−518.

(37) Ma, S.; et al. Enhanced sintering resistance of Fe_2O_3/CeO_2 oxygen carrier for chemical looping hydrogen generation using core-shell structure. *Int. J. Hydrogen Energy* **2019**, *44*, 6491−6504.

(38) Cabrera, N.; et al. Theory of the oxidation of metals. *Rep. Prog. Phys.* **1949**, *12*, 163.

(39) Himmel, L.; et al. Self-diffusion of iron in iron oixides and the Wagner theory of oxidation. *J. Metals* **1953**, *5*, 827−843.

(40) Millot, F.; et al. Diffusion of O18 in Fe_3O_4: an experimental approach to study the behavior of minority defects in oxides. *J. Phys. Chem. Solids.* **1997**, *58*, 63−72.

(41) Sharp, Z. D. Determination of oxygen diffusion rates in magnetite from natural isotopic variations. *Geology* **1991**, *19*, 653.

(42) Dieckmann, R.; et al. Defects and cation diffusion in magnetite (I). *Berichte der Bunsengesellschaft für physikalische Chemie* **1977**, *81*, 344−347.

(43) Smigelskas, A. D.; et al. Zinc diffusion in alpha-brass. *Transactions of the American Institute of Mining and Metallurgical Engineers* **1947**, *171*, 130−142.

(44) Yin, Y. D.; et al. Formation of hollow nanocrystals through the nanoscale Kirkendall Effect. *Science* **2004**, *304*, 711−714.

(45) Gonzalez, E.; et al. Carving at the Nanoscale: Sequential Galvanic Exchange and Kirkendall Growth at Room Temperature. *Science* **2011**, *334*, 1377−1380.

(46) Zhao, J. X.; et al. Tuning the CO_2 Hydrogenation Activity via Regulating the Strong Metal−Support Interactions of the Ni/Sm_2O_3 Catalyst. *ACS Catal.* **2024**, *14*, 3158−3168.

(47) Saunders, S. R. J.; et al. The oxidation behaviour of metals and alloys at high temperatures in atmospheres containing water vapour: A review. *Prog. Mater. Sci.* **2008**, *53*, 775−837.

(48) Li, L.; et al. Origins of large voltage hysteresis in high-energy-density metal fluoride lithium-ion battery conversion electrodes. *J. Am. Chem. Soc.* **2016**, *138*, 2838−2848.